Design of novel Zn-Ag-Zr alloy with enhanced strength as a potential biodegradable implant material

Wtroba, Maria; Bednarczyk, Wiktor; Kawako, Jakub; Mech, Krzysztof; Marciszko, Marianna; Boelter, Gabriela; Banzhaf, Manuel; Baa, Piotr

DOI:
10.1016/j.matdes.2019.108154

Materials and Design 183 (2019) 108154

Contents lists available at ScienceDirect

Materials and Design

journal homepage: www.elsevier.com/locate/matdes

Design of novel Zn-Ag-Zr alloy with enhanced strength as a potential biodegradable implant material

Maria Wątroba [a, *], Wiktor Bednarczyk [a], Jakub Kawałko [b], Krzysztof Mech [b], Marianna Marciszko [b], Gabriela Boelter [c], Manuel Banzhaf [c], Piotr Bała [a, b]

[a] AGH University of Science and Technology, Faculty of Metals Engineering and Industrial Computer Science, Al. A. Mickiewicza 30, 30-059 Krakow, Poland
[b] AGH University of Science and Technology, Academic Centre for Materials and Nanotechnology, Al. A. Mickiewicza 30, 30-059 Krakow, Poland
[c] Institute of Microbiology and Infection and School of Biosciences, University of Birmingham, Edgbaston, Birmingham B15 2TT, UK

HIGHLIGHTS

- Simultaneous additions of Ag and Zr result in solid solution strengthening and grain refinement by the presence of intermetallic $Zn_{22}Zr$ phase;
- Hot extruded Zn1Ag0.05Zr alloy shows enhanced strength and improved ductility in comparison to binary alloys;
- The designed Zn1Ag0.05Zr alloy exhibits biodegradation in Hanks' solution with corrosion rate 17.1 ± 1.0 μm/year;
- Investigated alloys from Zn-Ag-Zr system possess the ability to inhibit bacterial growth.

GRAPHICAL ABSTRACT

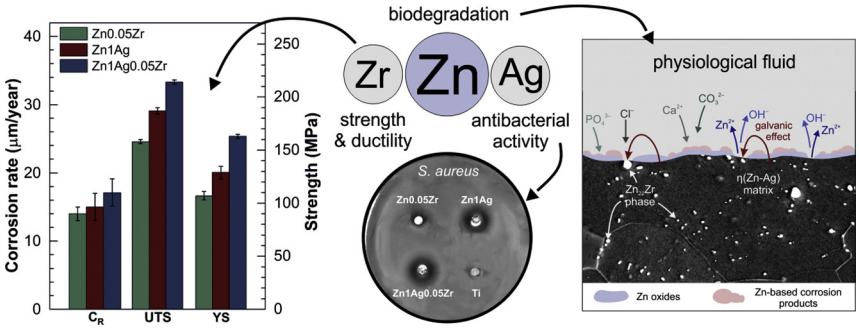

ARTICLE INFO

Article history:
Received 6 June 2019
Received in revised form
30 July 2019
Accepted 22 August 2019
Available online 26 August 2019

Keywords:
Zn-based alloy
Microstructure
Mechanical properties
Corrosion behavior
Biodegradable
Antimicrobial properties

Data availability:
The raw/processed data required to reproduce these findings cannot be shared at this time as the data also forms part of an ongoing study.

ABSTRACT

In this study, a new biodegradable alloy from the Zn-Ag-Zr system was investigated. Most importantly, mechanical properties and ductility were significantly improved in designed Zn1Ag0.05Zr alloy in comparison to binary Zn1Ag and previously investigated Zn0.05Zr alloys (wt%). The characterized alloy reached values of yield strength, ultimate tensile strength and elongation to failure equal to 166 ± 2 MPa, 211 ± 1 MPa and 35 ± 1%, respectively. Simultaneous addition of both alloying elements contributed to solid solution strengthening, intermetallic Zr-rich phase formation, and effective grain refinement. Immersion and electrochemical in vitro corrosion tests showed a slight increase of degradation rate in ternary alloy up to 17.1 ± 1.0 μm/year and no significant loss of mechanical properties after 28-day of immersion in simulated physiological solution. In addition, the preliminary antimicrobial studies show antimicrobial activity of the investigated Zn-Ag-Zr alloy against *Escherichia coli* and *Staphylococcus aureus*. The presented results demonstrate that newly developed Zn-based alloy can be considered as a promising biodegradable material for medical applications.

* Corresponding author.
E-mail address: mwatroba@agh.edu.pl (M. Wątroba).

https://doi.org/10.1016/j.matdes.2019.108154

1. Introduction

The interest in biodegradable metallic materials has been growing within the last ten years. So far, scientists focused their research efforts on magnesium, iron, zinc, and their alloys as promising, biocompatible materials for medical application. In addition, the research is driven by their potential application as biodegradable devices. During the regeneration of damaged tissue biodegradable implants slowly lose mechanical integrity and degrade in the environment of physiological fluids to completely dissolve in the human organism without surgical intervention. As suggested in the literature [1–3] the recommended daily amount of elements and ion concentrations in the human body can be considered as one of the characteristics to assess the biocompatibility. Taking into account the complexity of foreign body reactions to biomedical device, possible local ions accumulation at implementation sites, and formation of new compounds, they indicate that average amount of ions released during the biodegradation should not exceed the tolerable limits. Moreover, formed corrosion products cannot be harmful to the human body [4–6].

Therefore Zn-based alloys have attracted more attention in recent years. The main advantages of Zn are the following: (1) corrosion rate between Mg and Fe, (2) no hydrogen gas generation during degradation, (3) easy fabrication of cast products due to low melting temperature, (4) low reactivity during melting, (5) formation of non-harmful, biocompatible corrosion products [7,8]. Moreover, Zn is an essential element in human nutrition and cells proliferation and is also necessary in bone metabolism [9]. Recent investigations are focused on different fabrication techniques, conditions of plastic deformation processes and alloying with biocompatible elements that seem to address the fundamental issue related to poor mechanical properties and brittleness of pure Zn [10–12].

It was reported by Liu et al. [13,14] that in the as-cast state it is possible to refine the microstructure and simultaneously improve the strength and elongation to failure by additions of Mg, Al, Ag and Cu below their solubility limit in Zn. However, alloy systems with second phase precipitates give greater opportunities to modify the mechanical properties and corrosion rates. It was shown that elements such as Ag, Mg, Ca, Sr effectively increase the strength and ductility in the as-cast state by forming intermetallic precipitates [15,16]. Nevertheless, the mechanical properties of as-cast alloys usually do not meet the requirements to be considered for the use in medical devices. For this reason, current research refers mostly to binary or more complex alloys processed by extrusion, rolling or drawing [11] or fabricated by alternative methods like rapid solidification, additive manufacturing or powder metallurgy frequently aimed at obtaining porous scaffolds [17–20]. In accordance with the Hall-Petch relationship smaller grain size leads to obtaining higher strength [21]. That explains why other, unconventional low-temperature forming methods such as equal channel angular pressing [22,23], KoBo extrusion [24] or hydrostatic extrusion [25] are also applied to enhance mechanical properties of Zn alloys by significantly refining their microstructure. However, as it was reported in [26], severe plastic deformation process used for low-alloyed Zn alloys may be ineffective because the high grain refinement changes the deformation behavior to non-slip deformation mechanisms. In such case the activation of grain boundary sliding, viscous glide and creep results in lower YS and UTS, but much higher elongation to failure.

In this work, for the first time, the effect of Ag and Zr additions in Zn was examined. Based on the literature, Ag can strengthen the matrix by dissolution in Zn and also forms precipitates of Zn_3Ag hexagonal phase that results in grain refinement and mechanical properties enhancement [27,28]. Moreover, Ag stands out as an antibacterial element and in given concentration is nontoxic for human cells that is a valuable trait in medical applications. According to EPA Integrated Risk Information System the daily reference dose of Ag is evaluated as 5 μg/day per kilogram of body weight. Exceeding this limit, by a large amounts, can lead to argyria [29]. Zr, as almost insoluble element in Zn, forms intermetallic phases in Zn–Zr alloys [30]. It was reported that small Zr additions results in grain refinement, ductile fracture mode, and increase in strength in comparison to brittle pure Zn [31]. Zr exhibits good biocompatibility, low ionic cytotoxicity, good corrosion resistance and osteocompatibility similar to titanium [32,33]. Its average daily permissible intake should not exceed 50 μg/day [34]. To the best of our knowledge, investigation on Zn-Ag-Zr system is not reported in the literature so far. For the better understanding of the unique properties of Zn1Ag0.05Zr ternary alloy, it was compared in this work with Zn0.05Zr and Zn1Ag binary alloys.

To characterize the newly designed biodegradable alloy, the presented study contains a comprehensive overview of microstructure, mechanical properties, biodegradation behavior as well as the initial evaluation of antibacterial activity.

2. Experimental procedures

2.1. Materials processing and specimens preparation

The Zn0.05Zr, Zn1Ag, and Zn1Ag0.05Zr (wt%) alloys were fabricated by induction melting in a graphite crucible at 650 °C, followed by gravity casting into the steel mold. The high-purity alloying elements such as 99.995 wt% Zn, 99.995 wt% Ag, 99.95 wt % Zr were used to prepare the alloys. To homogenize the chemical composition and microstructure, release the stresses after the crystallization process and dissolve possible intermetallic phases precipitated after solidification, the 4 h solution treatment at 400 °C under air atmosphere followed by water quenching was applied. Subsequently, the homogenized ingots were processed by hot indirect extrusion at 250 °C, with extrusion speed 0.1 mm/s and extrusion ratio 25:1 to obtain rods with 4 mm of diameter.

2.2. Microstructural characterization

The microstructural observations of alloys in all states were performed on cross-sections perpendicular to pressing direction prepared by grinding with SiC papers up to #2000 grid and polishing with 3 and 1 μm alcohol-based diamond suspensions, and a final low-angle Ar^+ ion milling. Microstructural analysis was performed by means of NIKON ECLIPSE LV150N light microscope (LM), FEI VERSA 3D Scanning Electron Microscope (SEM) equipped with Energy Dispersive Spectroscopy (EDS) and Electron Back-Scattered Diffraction (EBSD) detectors. The average grain size, orientation maps, and textures for extruded samples were collected and processed by using *TSL OIM*™ software. The EBSD maps with 200 × 200 μm of size were collected using 0.3 μm step size. A grain was determined as a set of minimum 5 points with grain-to-grain misorientation angle higher than 15°.

2.3. Mechanical properties

Tensile and compression tests were used to evaluate the yield strength and ultimate tensile/compressive strength. Ductility of the investigated materials was characterized based on total elongation to failure, tensile fracture mode, and cross-sectional area reduction. Mechanical testing was performed using INSTRON 5966 universal testing machine at room temperature with strain rate $1 \times 10^{-3}\,s^{-1}$ and up to 50% of deformation during compression. Standard tensile specimens with a gauge length of 30 mm and gauge diameter of 3 mm were machined from rods according to ISO 6892-1 standard without any additional heat treatment. Total percent reduction in

cross-sectional area A_r was calculated based on the sample diameter measured in fractured region and in the initial state. Tensile fractures were analyzed by means of SEM. Samples for compression tests were cut out from rods and ground to obtain cylindrical specimens with initial dimensions 6 mm of height and 4 mm of diameter. Three samples were taken for each extruded alloy for both tests.

2.4. Biodegradation behavior

Biodegradation behavior and corrosion rate of the alloys were evaluated based on potentiodynamic measurements and static immersion tests in Hanks' solution of chemical composition presented in Table 1. The conductivity of deionized water used was 0.07 μS.

2.4.1. Electrochemical tests

Samples were cold mounted in epoxy resin and then ground down with SiC papers up to #2000 grit to reveal the longitudinal cross sections of rods with 1 cm^2 of the exposed area. Samples were then prepared for electrochemical tests by polishing with 3 and 1 μm alcohol-based diamond suspension. The samples were subsequently ultrasonically cleaned with ethanol and dried. Potentiodynamic polarization was performed with the use of a BioLogic SP300 potentiostat and *EC-Lab* software. The analysis was conducted using typical three-electrode flat-cell consisting of the sample as a working electrode, Ag/AgCl as a reference electrode and platinum as a counter electrode according to ASTM G5−94 standard. The electrochemical measurements were carried out at the scan rate of 1 mV s^{-1} in the electrochemical window starting from -200 mV to 200 mV versus Open Circuit Potential (OCP), at the controlled temperature of 37.5 ± 0.5 °C and pH value of the solution equal to 7.4 ± 0.1. Before the potentiodynamic polarization, each sample was immersed in Hanks' solution for 8 h to obtain the stabilization of open circuit potential. The corrosion current density was determined based on Tafel extrapolation and corrosion rate in μm/year was calculated according to ASTM-G102−89 standard. The parameters characterize corrosion behavior of tested alloys were determined with the use of *EC-Lab* software including built-in procedures and algorithms of curves fitting. The measurements were repeated three times for each alloy.

Surface morphology after electrochemical measurements was analyzed by SEM after removal of corrosion products. After 2 min of ultrasonic cleaning with chromate acid water solution (200 g/L of CrO_3) at 80 °C and the samples were cleaned with water, ethanol and air dried.

2.4.2. Immersion test

For immersion tests, samples were machined in the same way as for standard tensile test so as to investigate the change of tensile properties after corrosion testing. The preparation of each sample's surface was finished with ultrasonic cleaning in ethanol and drying. The samples were placed in separate closed-top containers at 37.5 ± 0.5 °C with 1 cm^2: 25 mL of surface area to Hanks' solution volume ratio in accordance with ASTM-G31−72 standard. The exposed surface area of investigated samples was about 6.5 cm^2. The corrosive medium was replaced every 2 days, to avoid significant changes in the pH value initially set as 7.4 ± 0.1 and increasing concentration of Zn^{2+}. After 28 days the samples were taken from Hanks' solution, cleaned with water, ethanol, and dried to characterize the surface morphology and formed corrosion products by SEM. After that the corrosion products were carefully removed from the surface by ultrasonic chemical cleaning with chromate acid (200 g/L of CrO_3) for about 2 min without removing any amount of metallic Zn, rinsing with water then ethanol, and drying. The surface morphology was then analyzed again by SEM. The corrosion rate (μm/year) was calculated based on the measured weight loss of three samples according to ASTM G1−90 standard.

2.5. Antimicrobial properties testing

In preparation for the experiments to investigate the antimicrobial property of examined materials, overnight cultures of *Escherichia coli* BW25113 (Gram-negative bacteria) and *Staphylococcus aureus* US300 (Gram-positive) were prepared. A single colony was inoculated with a sterile loop in 5 mL of Lysogeny broth (LB) (1% tryptone, 0.5% yeast extract, 0.5% NaCl) in sterile glassware. The cross-sections of the Zn alloys and Grade 2 titanium as a control sample were ground down to #2000, ultrasonically cleaned with ethanol and sterilized using an autoclave set to 15 min at 121 °C. 100 μL of the overnight culture was spread on Petri dishes containing LB agar and was allowed to dry for 15 min. The samples were placed on the agar plates with sterile tweezers. The plates were incubated for 16 h at 37 °C to test for antimicrobial properties of investigated materials. Endpoint pictures were taken using a camera and the bacterial growth inhibition was assessed based on measuring inhibition zone according to ISO 20645:2004 standard and the following equation:

$$H = \frac{D - d}{2} \quad (1)$$

where ***H*** is the inhibition zone (mm), ***D*** is the diameter of the sample and inhibition zone (mm), ***d*** is the diameter of the sample (mm). The H equal to or bigger than 1 mm is desirable value and indicates perfect antimicrobial behavior. The quantitative results of inhibition zone were averaged out from three samples for each alloy.

3. Results

3.1. Microstructural characterization

The microstructures of examined alloys in the as-cast, homogenized and extruded states are presented in Fig. 1. There are both polarized light microstructures to present the overall microstructure and SEM micrographs to distinguish the details. In Zn0.05Zr alloy the elongated, similar coarse grains are observed before and after homogenization process (Fig. 1a,d). There is no grain growth or second phase dissolution and precipitation during homogenization, which suggests that the alloy is thermodynamically stable. The visible small, white precipitates of the second phase, smaller than 5 μm, distributed in the whole volume of the material, indicated by white arrows, can be responsible for hindering the grain boundaries movement during annealing at 400 °C. Based on Zn−Zr phase diagram [30] and our previous research [31], especially EDS analysis, where the Zn to Zr atomic % ratio was about 22 in point measurements, it can be assumed that the Zr-rich phase occurring both in the Zn0.05Zr and Zn1Ag0.05Zr alloys has $Zn_{22}Zr$ stoichiometry. Zn1Ag and Zn1Ag0.05Zr alloys in the as-cast state feature the typical dendritic structure (Fig. 1b,c). After the homogenization

Table 1
Composition of Hanks' solution (per 1 L of deionized water).

$NaCl$	KCl	$CaCl_2$	$MgSO_4 \cdot 7H_2O$	$MgCl_2 \cdot 6H_2O$	Na_2HPO_4	KH_2PO_4	$NaHCO_3$	Glucose
8.0 g	0.4 g	0.14 g	0.1 g	0.1 g	0.06 g	0.06 g	0.35 g	1.0 g

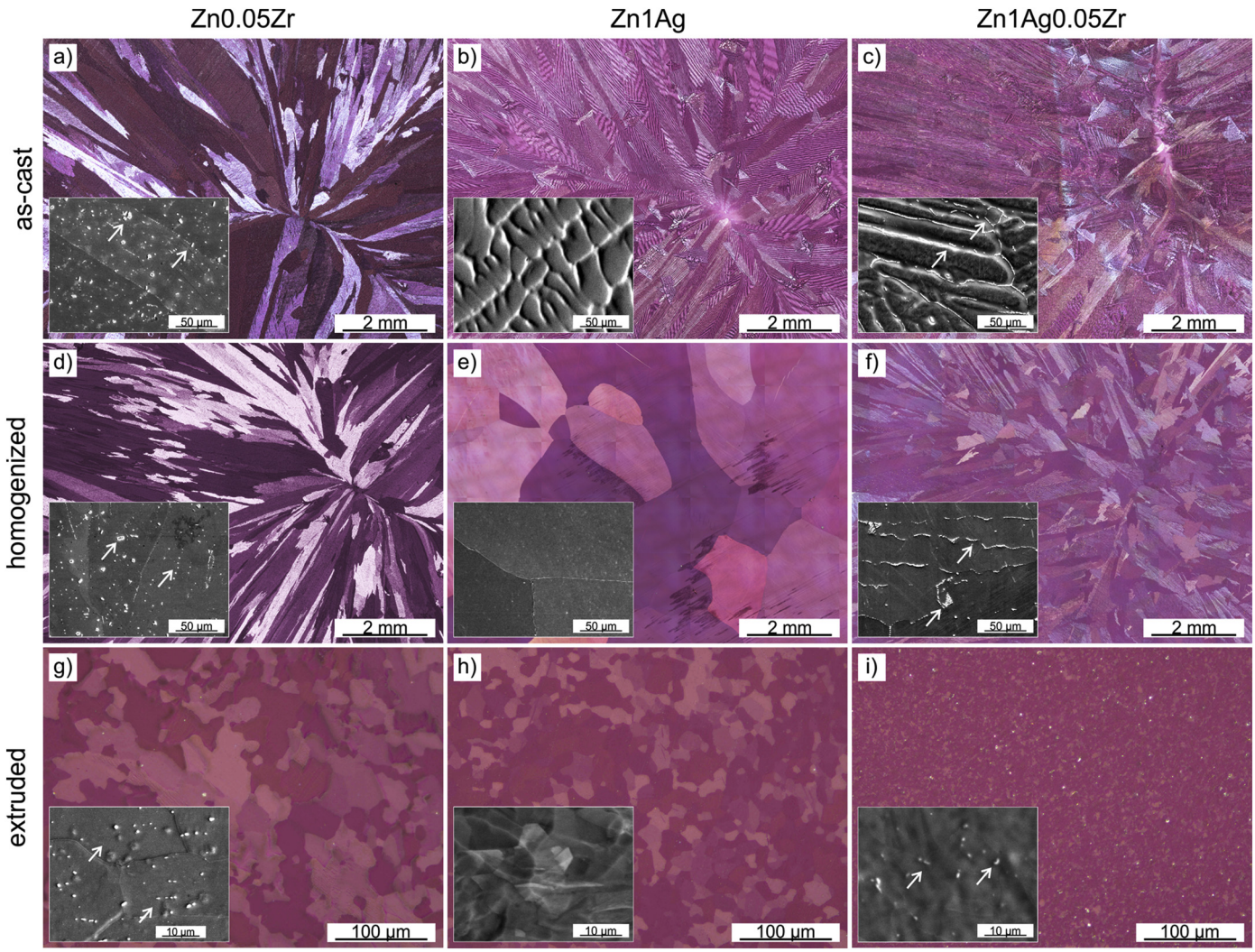

Fig. 1. Microstructures of Zn-0.05Zr (a, d, g), Zn−1Ag (b, e, h), Zn-1Ag-0.05Zr (c, f, i) in the as-cast, homogenized and extruded states, respectively. LM (polarized light), SEM. Please, note that the scale bar is different for the extruded state, because of refined microstructure in all alloys.

process the transition from the columnar microstructure to equiaxed grains occurs in Zn1Ag alloy (Fig. 1e). Presence of $Zn_{22}Zr$ precipitates between the dendrites arms in Zn1Ag0.05Zr alloy leads to stabilization of the microstructure during the annealing process (Fig. 1f).

As a result of the hot extrusion and dynamic recrystallization the finer, equiaxed grains with uniformly distributed precipitates of $Zn_{22}Zr$ phase, not exceeding hundreds of nanometers of size, appeared in the microstructure inside the grains and at the grain boundaries (Fig. 1g, h, j). It was additionally confirmed by X-ray diffraction technique, that Ag-rich phase did not precipitate in the extruded alloys. No peaks related to Zn_3Ag ε phase, were observed in measured XRD spectra indicating that Ag is dissolved in Zn matrix in Zn1Ag and Zn1Ag0.05Zr alloys in all states (see Supplementary Material). EDS analysis showed that the approximate content of Ag in Zn1Ag and Zn1Ag0.05Zr alloys was equal to 0.9 wt %, whereas in Zn0.05Zr and Zn1Ag0.05Zr the Zr content was about 0.5%. The overestimation of Zr might result from EDS limitations, its low concentration, and presence in $Zn_{22}Zr$ intermetallic phase instead of in solid solution, that generate relatively high error during quantitative analysis.

Based on EBSD orientation maps (Fig. 2a–c) it is evident that the simultaneous addition of Zr and Ag effectively influences the microstructure refinement. Average calculated grain size is equal to 42 ± 26 µm, 17 ± 8 µm, 10 ± 6 µm for Zn0.05Zr, Zn1Ag, Zn1Ag0.05Zr, respectively. Inverse pole figures (IPF) (Fig. 2d–f) show that all investigated alloys are characterized by fiber $(10\bar{1}0)$ texture typical for extruded Zn alloys [35].

3.2. Mechanical properties

In Fig. 3a the results of the tensile test are presented in form of engineering stress-strain curves. In order to determine the compressive strength the results of compression test are shown in Fig. 3b as true stress-strain curves. All the examined mechanical properties are summarized in Table 2. During tension, the Ag addition causes the higher yield strength (YS_T) and ultimate tensile strength (UTS) in comparison to Zn0.05Zr alloy. The desirable effect of both alloying elements can be observed in Zn1Ag0.05Zr alloy where YS_T and UTS reaches highest values among investigated alloys. Elongation to failure E_f is higher than 20% in all described materials and visible necking occurs during tension, which indicates good ductility.

Fracture morphologies shown in Fig. 4 confirm the ductile mode of deformation during tension. It can be seen that with increasing total elongation to failure the percent reduction of the area also increases (see Table 2). Fracture surfaces (Fig. 4d–f) consist of big holes and small dimples separated by sharp ridges caused by fine

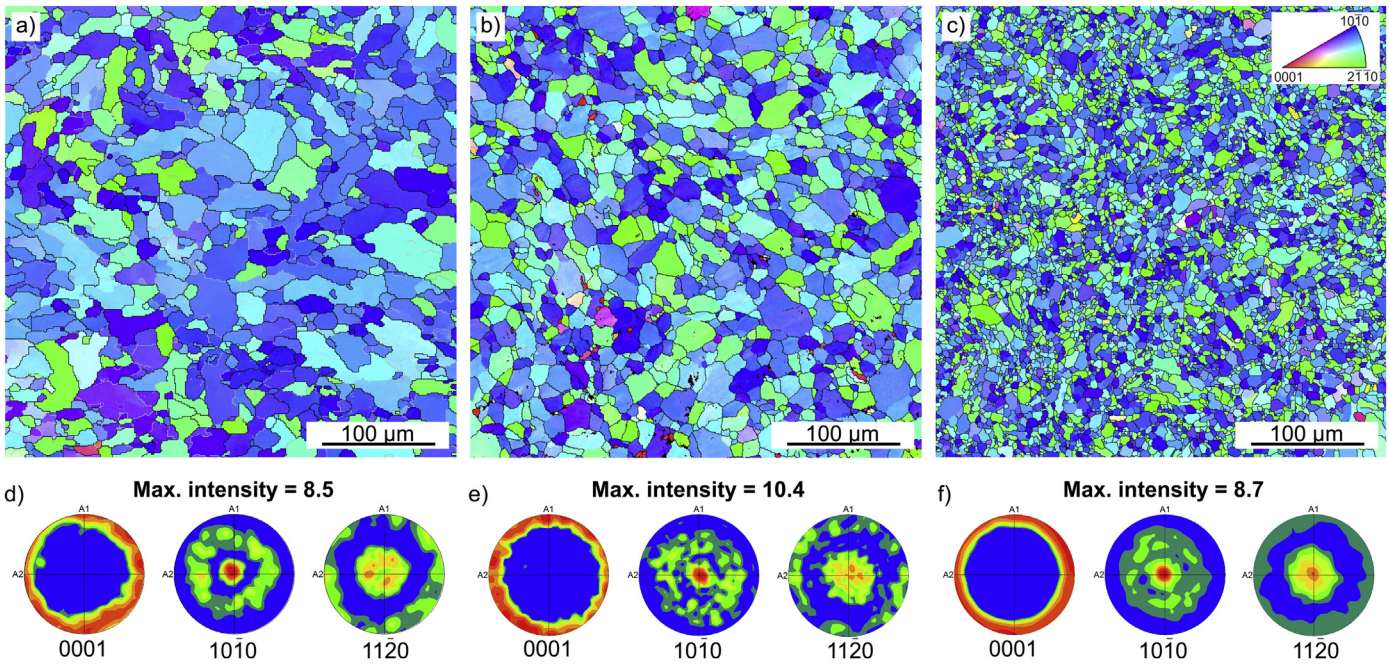

Fig. 2. EBSD-IPF orientation maps (a, b, c) and pole figures (d, e, f) of extruded materials: Zn0.05Zr (a, d), Zn1Ag (b, e), Zn1Ag0.05Zr (e, f).

equiaxed microstructure of investigated alloys. In addition, the features of Zn1Ag0.05Zr alloy fracture seems to be finer, because of initially smaller grain size in the microstructure. The $Zn_{22}Zr$ intermetallic phase precipitates were not observed to cause any crack initiation, but they might be acting as nucleation sites for some of the smaller dimples. No flat surfaces or facets, characteristic for brittle cracking were observed, indicating the $Zn_{22}Zr$ intermetallic phase precipitates did not cause any crack initiation, but they might be acting as nucleation sites for some of the smaller dimples.

The sharp textures and deformation mechanisms in hexagonal metals influence the apparent tension-compression asymmetry of strength [36]. Deformed samples achieve significantly higher values of yield strength during compression (YS_C). Ultimate compressive stress (UCS) in Zn1Ag and Zn1Ag0.05Zr are higher due to solid solution strengthening effect caused by Ag dissolved in Zn matrix and smaller grain size than in Zn0.05Zr alloy. The significant decrease of stresses after visible peak on the compression curves (Fig. 3b) indicates that dynamic recrystallization took place during further deformation.

Based on the shape of presented curves (Fig. 3b) and significant decrease of stresses after exceeding the deformation strain, at which the maximum compression stress occurred it can be assumed that dynamic recrystallization took place during further deformation.

3.3. Electrochemical tests

In Fig. 5a the curves of open circuit potential vs time for all extruded alloys immersed in Hanks' solution was presented. Within 8-hour OCP measurements the potential stabilization was achieved after 6 h and amounted to -0.978 ± 0.001 V, -0.988 ± 0.002 V, -0.976 ± 0.002 V for Zn0.05Zr, Zn1Ag and Zn1Ag0.05Zr alloys, respectively. The alloys with Zr addition are placed higher than Zn1Ag alloy, which suggests better corrosion resistance.

In Fig. 5b the potentiodynamic polarization curves were collected. Measurements show that the OCP of alloys with Ag addition are shifted to the more electronegative direction in comparison to Zn0.05Zr alloy, indicating an increased surface reactivity of those alloys. The shape of curves in the anodic range indicates the surface oxidation, which seems to occur at less electropositive potentials range in the case of Zn1Ag alloy. Further inflection of the binary alloys' curve at the so-called breakdown potential can come from pitting or dissolution of the samples. All materials possess a similar corrosion behavior in the cathodic side related to oxygen reduction reaction. An apparent increase of current density at more electronegative potentials indicates that water molecules are reduced in the solution resulting in hydrogen evolution [37,38].

Based on the SEM micrographs (Fig. 6), collected after electrochemical measurements and corrosion products removal, two different modes of corrosion can be distinguished such as continuous net of small pits and single large pits. The micrographs presented in the first row (Fig. 6a–c) correspond to the formation and growth of the oxidation layer during the experiments. Small, visible pits occur at sites of bare surface exposed to the solution after the further breakdown of this passivating film. In case of alloys with Zr addition, the additional random pits suggest the microgalvanic corrosion between Zn matrix and $Zn_{22}Zr$ precipitates. At the edge of the sample with slightly different kinetics of electrode reactions than in the middle part of the sample, bigger pits appeared (Fig. 6d-f). This can be explained by higher current density at the edges and more intensive dissolution of the alloys there, which is consistent with the polarization curves.

Corrosion current density and corrosion potential were evaluated by the Tafel extrapolation method. The characteristic parameters of potentiodynamic polarization curves and corrosion rate were summarized in Table 3. It can be seen that Ag addition increases the corrosion current density up to 12.3 ± 0.4 µm/cm^2, which results in 183.7 ± 21.1 µm/year of corrosion rate. However, the Zn1Ag0.05Zr alloy is characterized by the lowest short-term corrosion rate among tested alloys, obtained in electrochemical measurements amounting at 76.9 ± 33.3 µm/year. Number of factors influencing corrosion of the investigated alloys such as grain size, grain boundary density, presence of intermetallic precipitates and electrode potential of matrix in form of solid solution make it difficult to clearly predict final corrosion behavior and evaluate degradation rate in potentiodynamic measurements. It should be noted that observed differences in E_{corr} (Fig. 5b) and determined

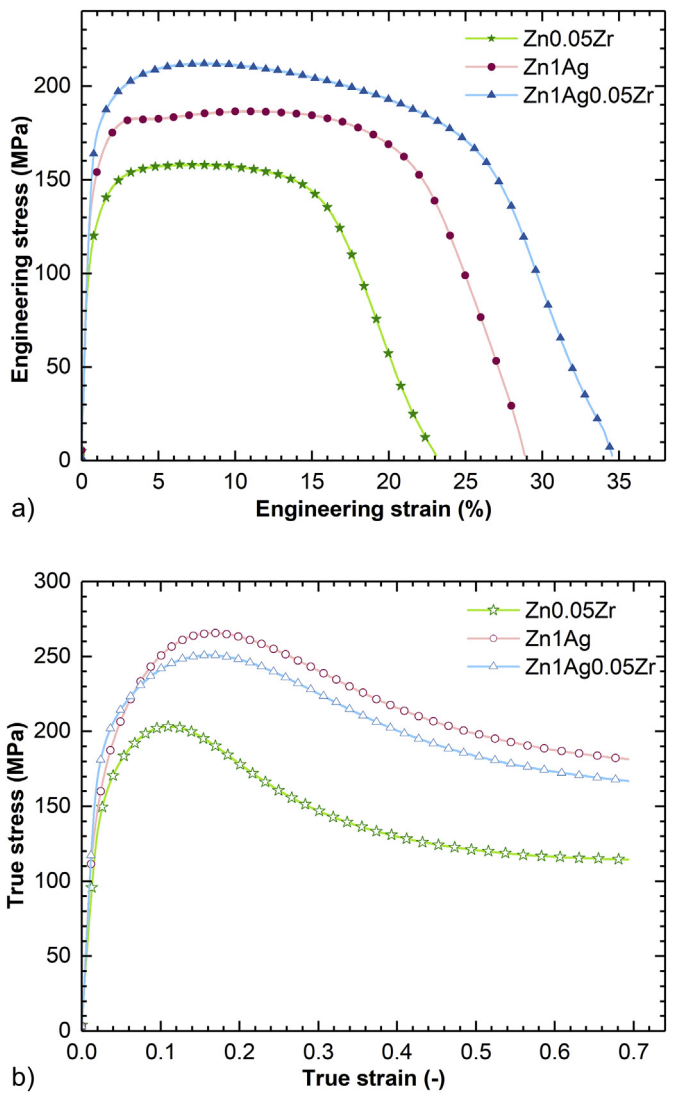

Fig. 3. Engineering tensile (a) and true compression (b) stress-strain curves of the extruded alloys.

OCP measurements (Fig. 5a) are very slight indicating similar corrosion behavior of the examined alloys. Parameters beyond i_{corr} not allowed on clear conclusions concerning influence of alloying elements on corrosion resistivity of the considered materials. That is why, long term static immersion test presented in next paragraph seems to be more accurate characterization technique in this case.

3.4. Immersion test

The corrosion rates determined based on mass loss after static immersion tests equal to 14.0 ± 0.1 μm/year and 15.0 ± 0.7 μm/year for Zn0.05Zr and Zn1Ag alloys, respectively. Simultaneous addition of both alloying elements resulted in an increase of corrosion rate by almost 20%, up to 17.1 ± 1.0 μm/year in Zn1Ag0.05Zr alloy. Differences in determined corrosion rates for several materials are related to changes in corrosion kinetics with time. Lower values of corrosion rates observed for long term immersion may result from limitation of corrosion process by passive layer formed at the alloy-electrolyte interface. Passivation process is additionally induced by microgalvanic corrosion due to presence of intermetallic phase in Zn matrix of different electronegativity.

Similar surface morphologies of the alloys exposed to Hanks' solution are presented in Fig. 7a–c. Compact layer of oxides as well as many white particles on top formed on the surface of the alloys. Because of internal stresses the corrosion layer is cracked and in the bare areas samples' surface is exposed to corrosive environment. An attempt was made to identify the corrosion products by X-ray analysis, but only peaks coming from η-Zn matrix and zinc oxide could be distinguished. This suggests that the thickness of the corrosion film is relatively small in comparison to base material and with used beam optics it was difficult to obtain meaningful intensive peaks from other compounds. The EDS analysis was performed to qualitatively assess the composition of corrosion products. Results presented in Table 4 may indicate that besides the basic elements of the alloys and oxides the corrosion products mostly consist of calcium, phosphorus, chloride, carbon, and magnesium originating from Hanks' solution. Based on the corrosion products analyzes and detected compounds presented in literature it can be supposed that observed degradation products are mainly zinc oxide (ZnO), zinc hydroxide ($Zn(OH)_2$) and probably some of more complex compounds such as hydroxides, phosphates, carbonates of zinc (calcium) [20,27,39–41].

After corrosion products removal, besides the evident scratches formed during samples preparation, many uniformly distributed corrosion pits can be observed on the surface (Fig. 7d–f).

To evaluate the influence of corrosion process on the loss of mechanical integrity the tensile test was repeated on samples after 28-day immersion in Hanks' solution and the results were collected in Table 5. A slight decrease in mechanical strength was observed.

3.5. Antibacterial behavior

Since the antimicrobial properties can reduce the risk of infections associated with implantation, which might have significant advantage for medical use, the attempt to evaluate the antimicrobial properties of presented alloys was additionally made in this work. The antimicrobial activity of described materials against the model bacteria *E.coli* (Gram-negative) and *S. aureus* (Gram-positive) was presented in Fig. 8. In comparison to titanium all Zn-based alloys possess antimicrobial activity. The growth inhibition zone was quantified using the referenced Eq. (1) and equals 1.9 ± 0.8, 3.9 ± 0.6, 2.9 ± 0.7 mm against *E. coli* and 2.2 ± 0.1, 4.5 ± 0.5, 3.9 ± 0.4 mm against *S. aureus* for Zn0.05Zr, Zn1Ag, Zn1Ag0.05Zr, respectively.

4. Discussion

4.1. Microstructure and mechanical properties

The addition of alloying elements and use of plastic deformation process was aimed at obtaining grain refinement, which in accordance with the mentioned-above Hall-Petch relation increased the strength of investigated alloys. A smaller grain size results in a

Table 2
Mechanical properties of extruded alloys.

Sample	Compression		Tension				
	YS_C (MPa)	UCS (MPa)	YS_T (MPa)	UTS (MPa)	E_f (%)	A_r (%)	UTS/YS_T (–)
Zn0.05Zr	134 ± 2	203 ± 4	104 ± 4	157 ± 1	22 ± 1	92	1.52
Zn1Ag	183 ± 1	266 ± 1	136 ± 6	183 ± 2	28 ± 1	95	1.35
Zn1Ag0.05Zr	168 ± 3	250 ± 3	166 ± 2	211 ± 1	35 ± 1	99	1.27

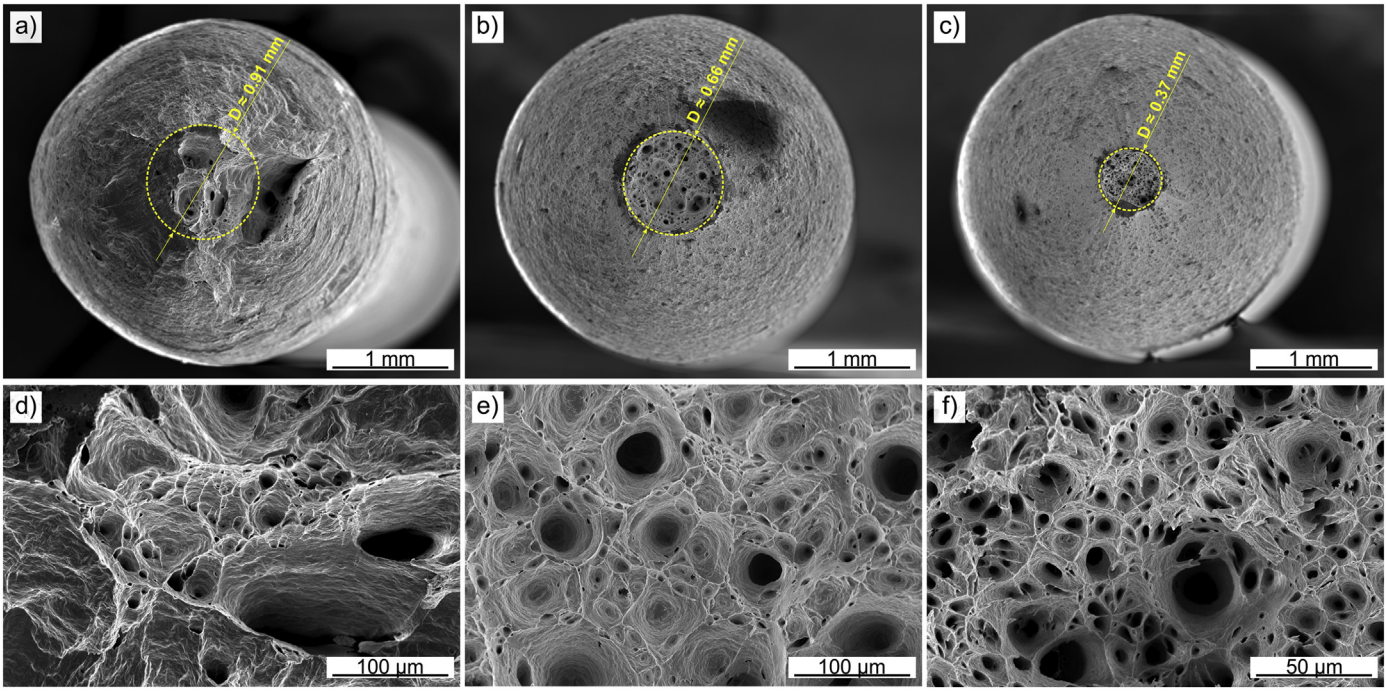

Fig. 4. Fracture morphologies of Zn0.05Zr (a, d), Zn1Ag (b, e), and Zn1Ag0.05Zr (e, f) alloys. SEM.

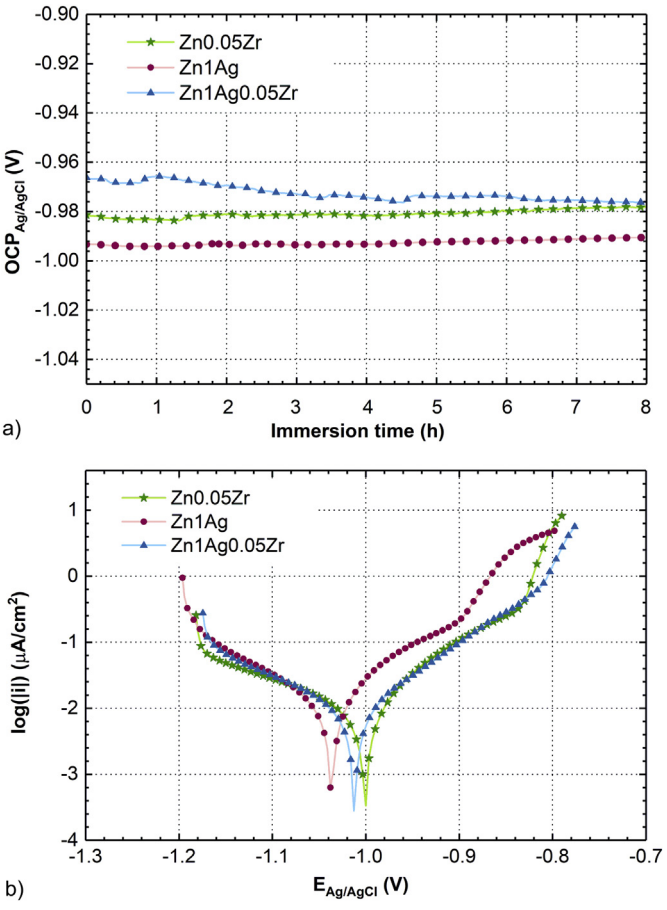

Fig. 5. Open circuit potential vs. time (a) and polarization curves (b) of the extruded alloys immersed in Hanks' solution at 37.5 °C.

larger amount of grain boundaries that creates an obstacle for dislocation movements and simultaneously enhances the strength of alloys. Grain size in extruded Zn1Ag0.05Zr alloy was reduced by approx. 76% and 41% in comparison to Zn0.05Zr and Zn1Ag alloys, respectively. Both in as-cast and extruded states it can be seen that Ag addition causes more effective grain refinement than Zr. It is consistent with previous reports that in the as-cast state, in the range of solubility, Ag noticeably reduces the grain size due to the high growth restriction factor of Ag in Zn [28]. The other mechanism behind grain refinement in Zn0.05Zr and Zn1Ag0.05Zr alloys mentioned in previous work can be the particle stimulated nucleation (PSN) [31]. During the extrusion higher stress zones form around $Zn_{22}Zr$ precipitates, which accelerate the dynamic recrystallization [43].

Presented mechanical properties (see Table 2) are significantly higher than ones reported in our previous work for extruded pure Zn ($YS_T = 68$ MPa, UTS = 110 MPa, $E_f = 8\%$) [31]. It is clear, that not only strength but also elongation to failure of pure Zn was improved. This suggests that simultaneous addition of both alloying elements resulted in solid solution strengthening and grain refinement. Hardening capacity is related to yield strength and further work hardening of the alloys and can be determined as a UTS to YS_T ratio. Grain refinement increases the yield strength and decreases hardening, which is consistent with the presented results. The Zn1Ag0.05Zr alloy exhibits the lowest and Zn0.05Zr alloy the highest UTS/YS_T ratio. It needs to be emphasized that Zn-based materials are characterized by relatively high strain rate sensitivity, so the results of mechanical properties are strongly dependent on applied strain rate during deformation [26]. This must be considered while comparing presented in the literature values of strength and elongation to failure for different Zn-based alloys.

Another significant factor affecting mechanical properties is the texture. The Zn1Ag alloy shows higher pole intensity of main peak in $10\bar{1}0$ pole figure than the other two alloys with Zr addition. This can be explained by the presence of $Zn_{22}Zr$ phase and PNS mechanism during recrystallization that weakens the texture [44]. No visible effect of a stronger texture of Zn1Ag alloy on tensile strength

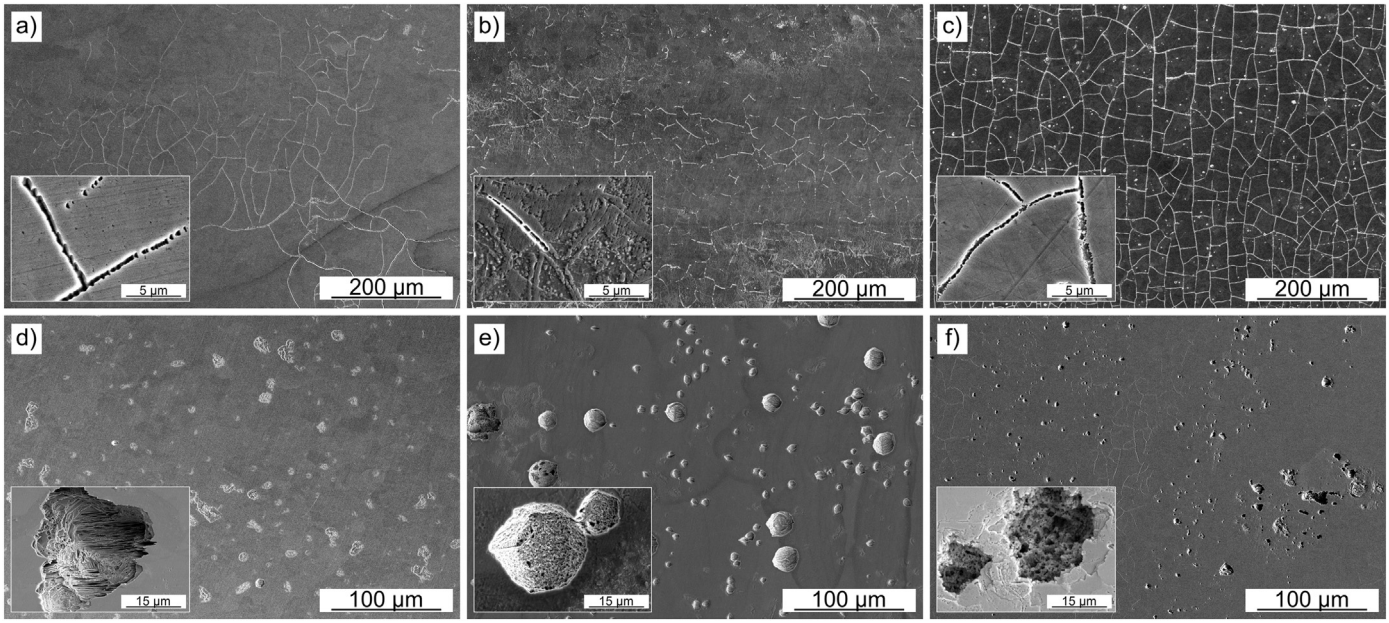

Fig. 6. SEM micrographs of the surface morphologies of (a, d) Zn0.05Zr, (b, e) Zn1Ag (c, f) Zn1Ag0.05Zr with removal of corrosion products after electrochemical measurements in Hanks' solution.

was noted, however Zn1Ag alloy showed the highest YS_C and UTS during compression (see Table 2). Asymmetry in tension-compression strength was observed in investigated alloys similar to other hexagonal metals. This can be explained by polar nature of twinning, which means that shear deformation is possible only in one direction other than in case of non-polar dislocation slip. Contrary to Mg alloys [45] Zn exhibits higher YS during compression than tension, which might be caused by higher c/a ratio of Zn crystal structure. What is interesting the higher value of UCS was noted for Zn1Ag in comparison to Zn1Ag0.05Zr alloy that generally exhibits higher tensile properties. This can result from mentioned above asymmetry of mechanical properties that was described in more detail in our recent research related to Zn-0.8Ag alloy [46]. In addition, almost two times smaller grain size in Zn1Ag0.05Zr, than in Zn1Ag alloy, hinders the most efficient strengthening mechanism, which is twinning. During the compression smaller number of twins cannot strengthen the Zn1Ag0.05Zr alloy as in alloys with bigger grains [47].

4.2. Corrosion properties

The next step in characterization of potential biodegradable implant material is an in vitro evaluation of the corrosion behavior and ability to uniform biodegradation in solution simulating body fluids. Corrosion tests were conducted in Hanks' solution, which is the most commonly used media for in vitro testing of biodegradable metals. The solution comprises a concentration of inorganic salts similar to those occurring in physiological fluids in human body.

In accordance with Pourbaix diagram, Zn in neutral or alkaline environment undergoes passivation [8]. The potentiodynamic polarization measurements confirmed that the passive layer forms on the surface of extruded alloys. It can be easily observed in Fig. 6 and Fig. 7 that the passive film is cracked and pits occur. This takes place even easier in the presence of Cl ions occurring in Hanks' solution [48]. The degradation process of Zn in neutral physiological environment is composed of anodic and cathodic reactions. Zhen et al. [39] described the corrosion process in form of electrochemical reactions with electrolyte as a general degradation mechanism for biodegradable metals. As a result of developing dissolution of Zn the pH of the solution increases, which is associated with a larger amount of OH ions. This leads to the formation of zinc oxides. As S. Zhao et al. reported [49] the presence of HCO_3^-, Cl^-, HPO_4^{2-} ions in physiological fluid, and also in Hanks' solution may be responsible for the formation of other phases along ZnO passive layer, such as zinc chloride hydroxide ($Zn_5(OH)_8Cl_2 \cdot H_2O$), zinc carbonate $ZnCO_3$ or calcium phosphate $Zn_3(PO_4)_2 \cdot 4(H_2O)$.

Based on current research and adequate literature the schematic model of biocorrosion of Zn1Ag0.05Zr alloy in Hanks' solution was proposed in Fig. 9.

Corrosion rates obtained for examined extruded alloys after 28-day immersion test are in the range between 14 and 17.1 μm/year, which is relatively low value in comparison to corrosion rates of other Zn alloys summarized in reviews [11,12] and much smaller than reported for Mg alloys [45]. Additionally, the corrosion rate for pure Zn in the same state and experimental conditions was investigated and equals 9.6 μm/year. As it was expected, the introduction of alloying elements increased the degradation rate. The possible explanation for that can be threefold (1) Ag dissolved in η(Zn) solid solution could change the standard electrode potential, accelerating corrosion process, which is consistent with shift of OCP towards more electronegative potentials as indicated by potentiodynamic polarization curves; (2) Ag as a solute element in Zn could introduce distortion in the crystal lattice and increase the corrosion rate due to stress corrosion; (3) Zr addition created sites for microgalvanic corrosion with anodic reaction localized at

Table 3
Electrochemical corrosion data for the extruded samples in Hanks' solution.

Sample	Corrosion potential, E_{corr} (V) vs. Ag/AgCl	Current density, i_{corr} (μA/cm^2)	Cathodic slope, β_c (mV)	Anodic slope, β_a (mV)	Corrosion rate, C_r (μm/year)
Zn1Ag	−1.035 ± 0.009	12.3 ± 0.4	156.0 ± 13.5	103.2 ± 13.5	183.7 ± 21.1
Zn1Ag0.05Zr	−1.008 ± 0.004	4.6 ± 2.2	212.9 ± 41.5	88.8 ± 11.8	76.9 ± 33.3

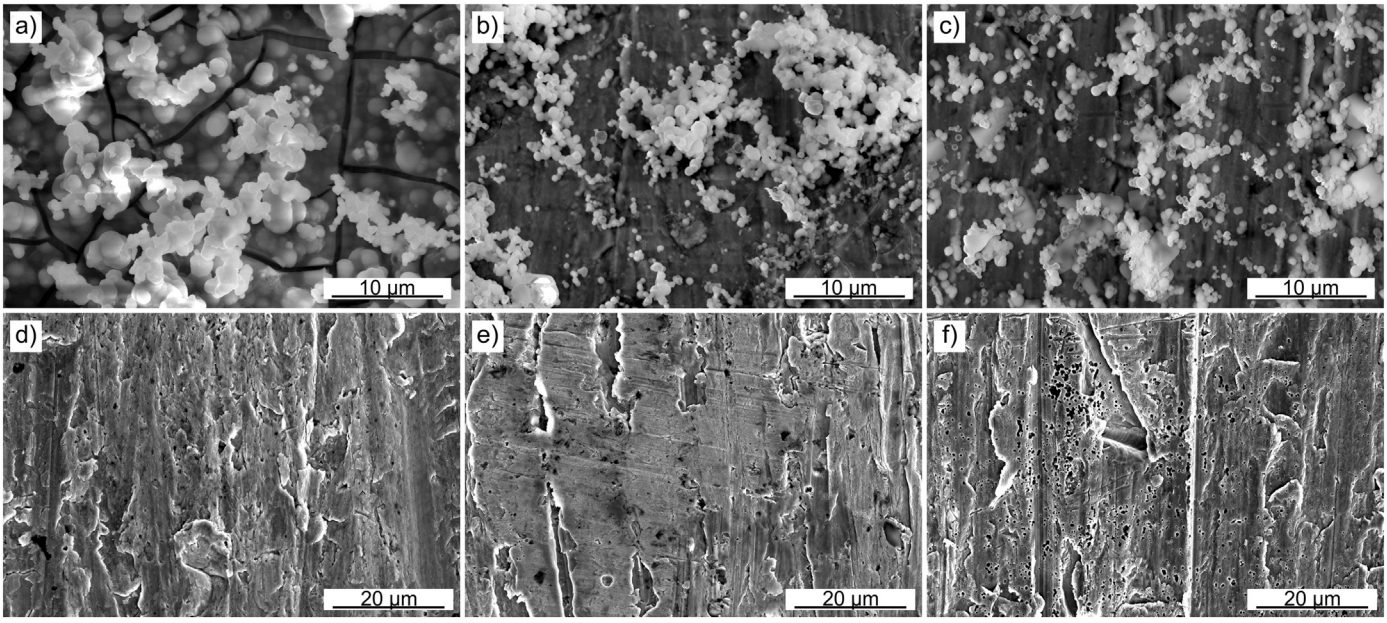

Fig. 7. SEM micrographs presenting the morphology of the corrosion products formed during immersion tests (a, b, c) and surface after cleaning the samples (d, e, f). Zn0.05Zr (a, d), Zn1Ag (b, e), Zn1Ag0.05Zr (c, f).

Zn matrix and cathodic ones localized at more electropositive $Zn_{22}Zr$ phase.

Sikora-Jasińska et al. show in [27] that the degradation rate for extruded Zn-xAg (x = 2.5, 5, 7 wt%) alloys in Hanks' solution is in the range of 79–84 μm/year. The difference can result from higher Ag concentration and presence of Zn_3Ag phase in microstructure of the alloy investigated there, contributing to microgalvanic corrosion process. Weight loss rate determined for Zn1Ag scaffold after 15-day of immersion in SBF (simulated body fluid) by Xie et al. [20] is equal to about 2.5%, while the value calculated for presented in this paper bulk sample of Zn1Ag is equal to about 0.14%. It is supposed that the main reason for apparently higher rate of weight loss for the same alloy, but in scaffold form is the presence of pores in the sample and much more developed surface exposed to corrosion environment. The increase of corrosion rate by Zr addition in Zn alloys stands in contrast to the effect of this element in Mg alloys. It was reported [45] that within and above the solubility range, Zr addition in Mg enhances the corrosion resistance in different simulated body fluid solutions. The opposite behavior can derive from the standard electrode potential of Zr (−1.45 V_{SCE}) that stands between the Zn (−0.762 V_{SCE}) and Mg (−2.372 V_{SCE}). Moreover, since Zr is a potent grain refiner in Mg alloys, by being active as nucleation centers, it creates a higher amount of grain boundaries, which can lead to deeper passivation process and simultaneously lower corrosion rate [50].

Surface analysis after corrosion products removal revealed uniformly distributed net of small pits, which is highly desired, because localized intensive corrosion in potential application could lead to rapid loss of mechanical integrity and failure of an implant. Biodegradable short-term implants should maintain sufficient strength during the regeneration time of damaged tissue. Presented slight loss of mechanical integrity in examined Zn alloys is much smaller than determined by Mostaed et al. for Zn–Mg, Zn–Al and Mg alloys in compression test [40] or by Li et al. for Mg-Zn-Zr alloy in tensile test (see the comparison in Table 5) [42]. It was surprising that the elongation to failure increased by a few percent in each alloy. It is believed that the main reason for this is the releasing of residual stresses formed in the surface after tensile samples machining because of elevated temperature (~37.5 °C) during the corrosion tests.

Due to mild biodegradation of investigated alloys, relatively short time of experiment and similar corrosion rates, it is supposed that obtained differences in mechanical properties result not as much from corrosion process, as from changes in the microstructure of samples due to elevated temperature (~37.5 °C) of the immersion test. Observed reduction of the tensile strength result from recrystallization of the deformed surface layer formed during the machining of samples. In the case of Zn0.05Zr alloy the effect is almost unnoticeable because the deformed layer recrystallizes at room temperature (RT ≈ 0.41T_m, where T_m is absolute melting temperature of pure Zn), before initial tensile testing. The recrystallization of deformed layer in Zn1Ag and Zn1Ag0.05Zr alloys is partially hindered at RT due to Ag addition dissolved in the Zn matrix [51], resulting in slightly increased strenght measured before the immersion test. The complete recrystallization of the deforation layer in the case of alloys with Ag addition occurs during the immersion test at 37.5 °C which results in apparent YS and UTS decrease. However, the effect is more visible in Zn1Ag alloy because bigger grain size results in thicker deformed layer and higher strengthening effect of twinning. Ultimately, slight loss of mechanical strength and ductility is a desirable result after 28-day of corrosion testing. It would not be good to observe sudden decrease

Table 4
EDS results of the corrosion products formed on investigated samples during immersion tests.

Element [wt%]	Zn	O	C	Mg	P	Zr	Cl	Ag	Ca
Zn0.05Zr	37.7	21.2	2.4	2.5	12.3	3.2	0.4	–	20.3
Zn1Ag	64.2	19.8	1.2	1.2	6.6	–	0.0	0.5	4.1
Zn1Ag0.05Zr	60.9	17.1	0.5	0.9	7.9	1.8	2.1	0.5	8.4

Table 5
Mechanical properties reduction of alloys after immersion tests.

Sample	Reduction in YS_T (%)	Reduction in UTS (%)
Zn0.05Zr	0.9	1.2
Zn1Ag	7.0	1.6
Zn1Ag0.05Zr	4.1	2.1
Zn-3 Mg	8.2	← compressive yield strength [40]
Zn0.5Al	8.7	
AZ31 alloy	45.3	
Mg3.2Zn0.8Zr	44.2	32.7 [42]

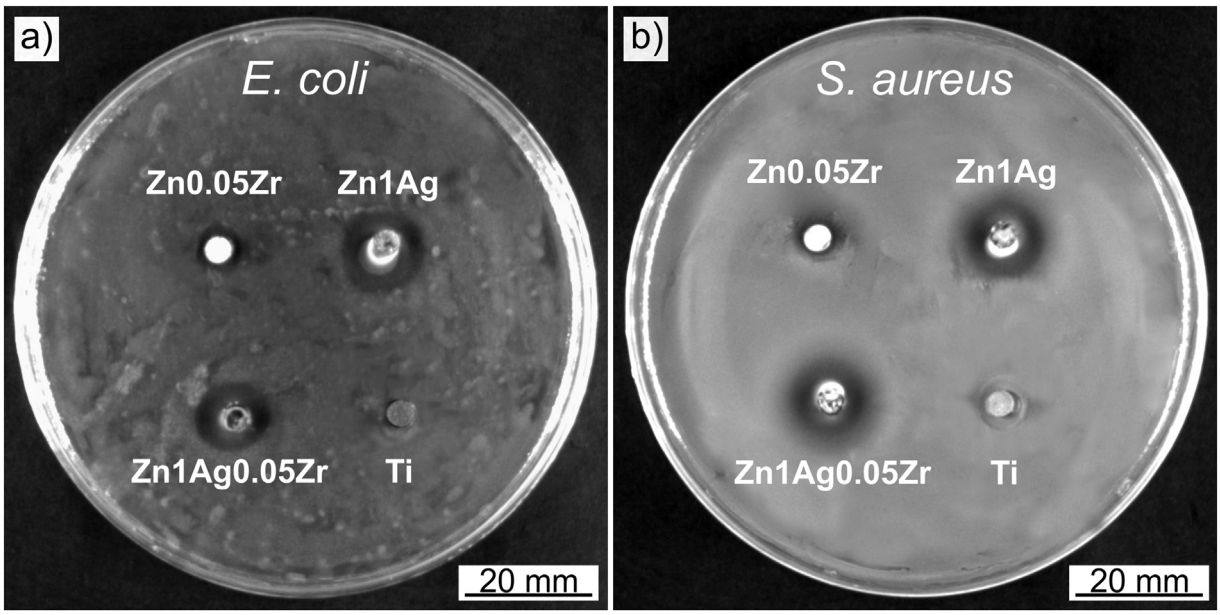

Fig. 8. The digital photos of inhibition zone of Zn0.05Zr, Zn1Ag, Zn1Ag0.05Zr and Ti samples for co-cultured a) *E.coli* and b) *S. aureus* on agar plates.

of mechanical properties after this relatively short time of degradation.

The average weight loss calculated for Zn0.05Zr, Zn1Ag, and Zn1Ag0.05Zr alloy is equal to 5.5 mg, 5.9 mg, 6.7 mg respectively. Hence, mean loss for investigated alloys is approx. 0.22 mg/day, which is much less than 40 mg/day of acceptable daily intake limit of Zn by the human body. Furthermore, because of small concentrations of alloying elements and relatively slow biodegradation, there is nearly no risk that releasing Ag and Zr ions will exceed the acceptable limits. However, it has to be emphasized, that these values are highly dependent on the analyzed surface area that is in contact with the corrosive environment, so the real value of daily weight loss and the amount of releasing ions need to be considered based on the final geometry of the implant.

4.3. Antibacterial effect

It was reported that Zn can prevent bacterial growth and biofilm formation for several pathogenic bacteria [52]. Research presented by Li et al. [15] and Xie et al. [20] confirm an antimicrobial effect in Zn—Ag alloys. It was shown that materials releasing Ag ions inhibit the propagation of microorganism such as bacteria, yeasts, viruses, and fungi [53]. Zr also possesses antimicrobial activity by preventing bacterial colonization on the surfaces [54]. However, the synergic antimicrobial effect of Zn, Ag and Zr ions in ternary alloy presented in this study has not been described yet. The inhibition zone, in the margin of error, for Zn1Ag0.05Zr alloy is not bigger than for Zn1Ag binary alloy. One explanation for this can be similarly slow degradation rates of investigated materials. This affects the released ions that ultimately stop propagation of bacteria. More work needs to be done to understand this dependence. Nevertheless, in comparison to Ti grade 2 reference sample, the observed antimicrobial activity for alloys is substantial and therefore the examined alloys can be considered for medical application.

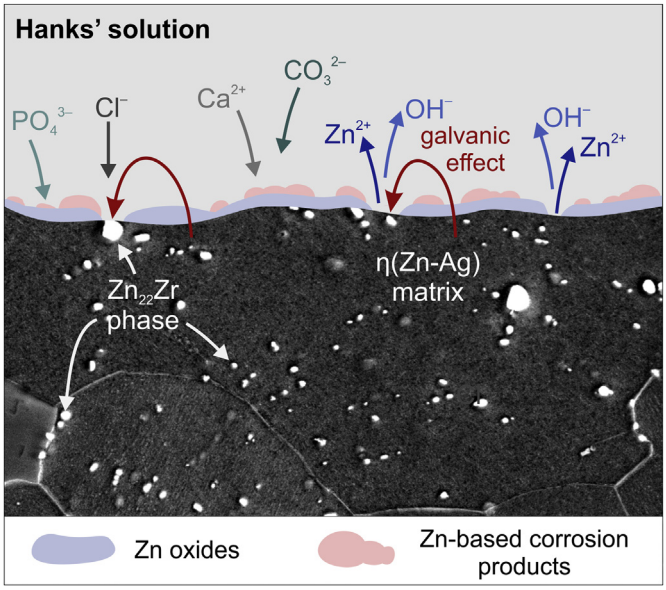

Fig. 9. Schematic model for biocorrosion of Zn1Ag0.05Zr alloy in Hanks' solution.

5. Conclusions

In this study newly designed Zn-based ternary alloy has been investigated. For the first time the microstructure, mechanical properties, corrosion behavior, and preliminary antimicrobial activity were described for Zn1Ag0.05Zr alloy. Besides microstructure analysis performed in all states, both Zn1Ag0.05Zr alloy and two reference binary Zn0.05Zr, Zn1Ag alloys were further examined in extruded state. Being aware of in vitro study limitations the following conclusions can be drawn based on presented results:

1. Both Zr and Ag cause noticeable grain refinement. Simultaneous addition of both alloying elements results in the smallest grain size up to about 10 μm in samples after the extrusion process.
2. Zr addition forms precipitates of second intermetallic $Zn_{22}Zr$ phase, inhibiting grain growth after recrystallization during the extrusion process, while Ag addition dissolves in Zn matrix and causes solid solution strengthening.
3. All investigated alloys in the extruded state are characterized by ductile behavior during deformation. Zn1Ag0.05Zr alloy exhibits the highest mechanical properties, such as 166 ± 2 MPa of yield strength, 211 ± 1 MPa of ultimate tensile strength and 35 ± 1% of the elongation to failure.

4. Corrosion tests showed that all extruded alloys degrade relatively slowly in Hanks' solution. In comparison to binary Zn0.05Zr and Zn1Ag alloys, the addition of both alloying elements in Zn1Ag0.05Zr alloy results in a slight increase of corrosion rate and equal to 17.1 ± 0.1 μm/year after 28-day static immersion test. The same trend was observed in electrochemical measurements. Uniformly distributed small pits formed on the surface of degraded samples, which means that intensive galvanic corrosion between Zn matric and $Zn_{22}Zr$ phase did not occur. A very small decrease in mechanical properties after the static corrosion test was observed.
5. Examined alloys exhibit antibacterial activity against both *Escherichia coli* and *Staphylococcus aureus*. It was shown, that Ag addition enlarges the bacteria growth inhibition zone for Zn1Ag and Zn1Ag0.05Zr alloys.

Presented results strongly indicate that examined materials, especially ternary Zn1Ag0.05Zr alloy, can be considered as a promising biodegradable metallic material for stents or fracture fixations. Additional improvement of mechanical properties could be obtained by the change of extrusion conditions or applying heat treatment. Further in vitro studies related to cytotoxicity and cell proliferation as well as more detailed microbial tests are required for full characterization of biological activity of designed Zn-based alloys.

Supplementary data to this article can be found online at https://doi.org/10.1016/j.matdes.2019.108154.

Acknowledgment

This work was supported by the Polish National Science Centre [Grant number 2018/29/N/ST8/01703].

References

[1] D. Vojtěch, J. Kubásek, J. Šerák, P. Novák, Mechanical and corrosion properties of newly developed biodegradable Zn-based alloys for bone fixation, Acta Biomater. 7 (2011) 3515–3522, https://doi.org/10.1016/j.actbio.2011.05.008.
[2] J.M. Seitz, M. Durisin, J. Goldman, J.W. Drelich, Recent advances in biodegradable metals for medical sutures: a critical review, Adv. Healthc. Mater. 4 (2015) 1915–1936, https://doi.org/10.1002/adhm.201500189.
[3] C. Shuai, S. Li, S. Peng, P. Feng, Y. Lai, C. Gao, Biodegradable metallic bone implants, Mater. Chem. Front. 3 (2019) 544–562, https://doi.org/10.1039/c8qm00507a.
[4] M. Moravej, D. Mantovani, Biodegradable metals for cardiovascular stent application: interests and new opportunities, Int. J. Mol. Sci. 12 (2011) 4250–4270, https://doi.org/10.3390/ijms12074250.
[5] H. Han, S. Loffredo, I. Jun, J. Edwards, Y. Kim, H. Seok, F. Witte, D. Mantovani, S. Glyn-jones, Current status and outlook on the clinical translation of biodegradable metals, Mater. Today 23 (2019) 57–71, https://doi.org/10.1016/j.mattod.2018.05.018.
[6] M.H. Emily Walker, Magnesium, iron and zinc alloys, the trifecta of bioresorbable orthopaedic and vascular implantation - a review, J. Biotechnol. Biomater. 5 (2015) 1–9, https://doi.org/10.4172/2155-952X.1000178.
[7] P.K. Bowen, J. Drelich, J. Goldman, Zinc exhibits ideal physiological corrosion behavior for bioabsorbable stents, Adv. Mater. 25 (2013) 2577–2582, https://doi.org/10.1002/adma.201300226.
[8] P.K. Bowen, E.R. Shearier, S. Zhao, R.J.G. Ii, F. Zhao, J. Goldman, J.W. Drelich, Biodegradable Metals for Cardiovascular Stents: from Clinical Concerns to Recent Zn-alloys, 2016, pp. 1121–1140, https://doi.org/10.1002/adhm.201501019.
[9] H. Tapiero, K.D. Tew, Trace elements in human physiology and pathology: zinc and metallothioneins, Biomed. Pharmacother. 57 (2003) 399–411, https://doi.org/10.1016/S0753-3322(03)00081-7.
[10] Z. Liu, A new approach toward designing and synthesizing the microalloying Zn biodegradable alloys with improved mechanical properties, Metall. Mater. Trans. A. 50 (2019) 311–325, https://doi.org/10.1007/s11661-018-4978-4.
[11] J. Venezuela, M.S. Dargusch, The influence of alloying and fabrication techniques on the mechanical properties, biodegradability and biocompatibility of zinc: a comprehensive review, Acta Biomater. 15 (2019) 1–40, https://doi.org/10.1016/j.actbio.2019.01.035.
[12] E. Mostaed, M. Sikora-Jasinska, J.W. Drelich, M. Vedani, Zinc-based alloys for degradable vascular stent applications, Acta Biomater. 71 (2018) 1–23, https://doi.org/10.1016/J.ACTBIO.2018.03.005.
[13] Z. Liu, D. Qiu, F. Wang, J.A. Taylor, M. Zhang, Effect of grain refinement on tensile properties of cast zinc alloys, Metall. Mater. Trans. A. 47A (2016) 830–841, https://doi.org/10.1007/s11661-015-3229-1.
[14] Z. Liu, F. Wang, D. Qiu, J.A. Taylor, M. Zhang, The effect of solute elements on the grain refinement of cast Zn, Metall. Mater. Trans. A - Phys. Metall. Mater. Sci. 44 (2013) 4025–4030, https://doi.org/10.1007/s11661-013-1861-1.
[15] P. Li, C. Schille, E. Schweizer, F. Rupp, A. Heiss, C. Legner, U.E. Klotz, J.G. Gerstorfer, L. Scheideler, Mechanical characteristics, in vitro degradation, cytotoxicity, and antibacterial evaluation of Zn-4.0Ag alloy as a biodegradable material, Int. J. Mol. Sci. 19 (2018) 1–15, https://doi.org/10.3390/ijms19030755.
[16] H.F. Li, X.H. Xie, Y.F. Zheng, Y. Cong, F.Y. Zhou, K.J. Qiu, X. Wang, S.H. Chen, L. Huang, L. Tian, L. Qin, Development of biodegradable Zn-1X binary alloys with nutrient alloying elements Mg, Ca and Sr, Sci. Rep. 5 (2015), 10719, https://doi.org/10.1038/srep10719.
[17] C. Shuai, Y. Cheng, Y. Yang, S. Peng, W. Yang, Laser additive manufacturing of Zn-2Al part for bone repair: formability, microstructure and properties, J. Alloys Compd. 798 (2019) 606–615, https://doi.org/10.1016/j.jallcom.2019.05.278.
[18] Y. Yang, F. Yuan, C. Gao, P. Feng, L. Xue, S. He, C. Shuai, A combined strategy to enhance the properties of Zn by laser rapid solidification and laser alloying, J. Mech. Behav. Biomed. Mater. 82 (2018) 51–60, https://doi.org/10.1016/j.jmbbm.2018.03.018.
[19] Y. Qin, P. Wen, M. Voshage, Y. Chen, P.G. Schückler, L. Jauer, D. Xia, H. Guo, Y. Zheng, J.H. Schleifenbaum, Additive manufacturing of biodegradable Zn-xWE43 porous scaffolds: formation quality, microstructure and mechanical properties, Mater. Des. 181 (2019), 107937, https://doi.org/10.1016/j.matdes.2019.107937.
[20] Y. Xie, L. Zhao, Z. Zhang, X. Wang, C. Cui, Fabrication and properties of porous Zn-Ag alloy scaffolds as biodegradable materials, Mater. Chem. Phys. 219 (2018) 433–443, https://doi.org/10.1016/j.matchemphys.2018.08.023.
[21] E.O. Hall, The deformation and ageing of mild steel. III discussion of results, Proc. Phys. Soc. Lond. 64 (1951) 747–753, https://doi.org/10.1088/0370-1301/64/9/303.
[22] M.S. Dambatta, S. Izman, D. Kurniawan, H. Hermawan, Processing of Zn-3Mg alloy by equal channel angular pressing for biodegradable metal implants, J. King Saud Univ. - Sci. 29 (2017) 455–461, https://doi.org/10.1016/j.jksus.2017.07.008.
[23] W. Bednarczyk, J. Kawałko, M. Wątroba, P. Bała, Achieving room temperature superplasticity in the Zn-0.5Cu alloy processed via equal channel angular pressing, Mater. Sci. Eng. A 723 (2018) 126–133, https://doi.org/10.1016/j.msea.2018.03.052.
[24] K. Pieła, M. Wróbel, K. Sztwiertnia, M. Jaskowski, J. Kawałko, M. Bieda, M. Kiper, A. Jarzębska, Zinc subjected to plastic deformation by complex loading and conventional extrusion: comparison of the microstructure and mechanical properties, Mater. Des. 117 (2017) 111–120, https://doi.org/10.1016/j.matdes.2016.12.056.
[25] A. Jarzębska, M. Bieda, J. Kawałko, P. Koprowski Rogal, K. Sztwiertnia, W. Pachla, M. Kulczyk, A new approach to plastic deformation of biodegradable zinc alloy with magnesium and its effect on microstructure and mechanical properties, Mater. Lett. 211 (2018) 58–61, https://doi.org/10.1016/j.matlet.2017.09.090.
[26] W. Bednarczyk, M. Wątroba, J. Kawałko, P. Bała, Can zinc alloys be strengthened by grain refinement? A critical evaluation of the processing of low-alloyed binary zinc alloys using ECAP, Mater. Sci. Eng. A 748 (2019) 357–366, https://doi.org/10.1016/J.MSEA.2019.01.117.
[27] M. Sikora-Jasinska, E. Mostaed, A. Mostaed, R. Beanland, D. Mantovani, M. Vedani, Fabrication, mechanical properties and in vitro degradation behavior of newly developed ZnAg alloys for degradable implant applications, Mater. Sci. Eng. C. 77 (2017) 1170–1181, https://doi.org/10.1016/j.msec.2017.04.023.
[28] Z. Liu, D. Qiu, F. Wang, J.A. Taylor, M. Zhang, The grain refining mechanism of cast zinc through silver inoculation, Acta Mater. 79 (2014) 315–326, https://doi.org/10.1016/j.actamat.2014.07.026.
[29] N. Hadrup, H.R. Lam, Oral toxicity of silver ions, silver nanoparticles and colloidal silver – a review, Regul. Toxicol. Pharmacol. 68 (2014) 1–7, https://doi.org/10.1016/j.yrtph.2013.11.002.
[30] J. Dutkiewicz, The Zn-Zr (zinc-zirconium) system, J. Phase Equilibria. 13 (1992) 430–433.
[31] M. Wątroba, W. Bednarczyk, J. Kawałko, P. Bała, Effect of zirconium microaddition on the microstructure and mechanical properties of Zn-Zr alloys, Mater. Charact. 142 (2018) 187–194, https://doi.org/10.1016/j.matchar.2018.05.055.
[32] E. Eisenbarth, D. Velten, M. M, Biocompatibility of b -stabilizing elements of titanium alloys, Biomaterials 25 (2004) 5705–5713, https://doi.org/10.1016/j.biomaterials.2004.01.021.
[33] Y. Ding, J. Lin, C. Wen, D. Zhang, Y. Li, Mechanical properties, in vitro corrosion and biocompatibility of newly developed biodegradable Mg-Zr-Sr-Ho alloys for biomedical applications, Sci. Rep. 6 (2016) 1–10, https://doi.org/10.1038/srep31990.
[34] D. Hong, P. Saha, D.T. Chou, B. Lee, B.E. Collins, Z. Tan, Z. Dong, P.N. Kumta, In vitro degradation and cytotoxicity response of Mg-4% Zn-0.5% Zr (ZK40) alloy as a potential biodegradable material, Acta Biomater. 9 (2013) 8534–8547, https://doi.org/10.1016/j.actbio.2013.07.001.
[35] Y.N. Wang, J.C. Huang, Texture analysis in hexagonal materials, Mater. Chem. Phys. 81 (2003) 11–26, https://doi.org/10.1016/S0254-0584(03)00168-8.
[36] J.J. Fundenberger, M.J. Philippe, F. Wagner, C. Esling, Modelling and prediction

of mechanical properties for materials with hexagonal symmetry (zinc, titanium and zirconium alloys), Acta Mater. 45 (1997) 4041–4055, https://doi.org/10.1016/S1359-6454(97)00099-2.
[37] Y. Chen, W. Zhang, M.F. Maitz, M. Chen, H. Zhang, J. Mao, Y. Zhao, N. Huang, G. Wan, Comparative corrosion behavior of Zn with Fe and Mg in the course of immersion degradation in phosphate buffered saline, Corros. Sci. 111 (2016) 541–555, https://doi.org/10.1016/j.corsci.2016.05.039.
[38] M. Bobby Kannan, C. Moore, S. Saptarshi, S. Somasundaram, M. Rahuma, A.L. Lopata, Biocompatibility and biodegradation studies of a commercial zinc alloy for temporary mini-implant applications, Sci. Rep. 7 (2017) 1–11, https://doi.org/10.1038/s41598-017-15873-w.
[39] Y.F. Zheng, X.N. Gu, F. Witte, Biodegradable metals, Mater. Sci. Eng. R Reports. 77 (2014) 1–34, https://doi.org/10.1016/j.mser.2014.01.001.
[40] E. Mostaed, M. Sikora-Jasinska, A. Mostaed, S. Loffredo, A.G. Demir, B. Previtali, D. Mantovani, R. Beanland, M. Vedani, Novel Zn-based alloys for biodegradable stent applications: design, development and in vitro degradation, J. Mech. Behav. Biomed. Mater. 60 (2016) 581–602, https://doi.org/10.1016/j.jmbbm.2016.03.018.
[41] X. Liu, J. Sun, F. Zhou, Y. Yang, R. Chang, K. Qiu, Z. Pu, Micro-alloying with Mn in Zn − Mg alloy for future biodegradable metals application, Mater. Des. 94 (2016) 95–104, https://doi.org/10.1016/j.matdes.2015.12.128.
[42] Z. Li, S. Shizhao, M. Chen, B.D. Fahlman, H. Bi Debao Liu, In vitro and in vivo corrosion, mechanical properties and biocompatibility evaluation of MgF2-coated Mg-Zn-Zr alloy as cancellous screws, Mater. Sci. Eng. C. 75 (2017) 1268–1280, https://doi.org/10.1016/j.msec.2017.02.168.
[43] J. Kubásek, D. Vojt, I. Pospíšilová, A. Michalcová, J. Maixner, Microstructure and mechanical properties of the micrograined hypoeutectic Zn − Mg alloy, Int. J. Miner. Metall. Mater. 23 (2016) 1167–1176, https://doi.org/10.1007/s12613-016-1336-7.
[44] L.W.F. Mackenzie, M.O. Pekguleryuz, The recrystallization and texture of magnesium-zinc-cerium alloys, Scr. Mater. 59 (2008) 665–668, https://doi.org/10.1016/j.scriptamat.2008.05.021.
[45] P. Saha, M. Roy, M.K. Datta, B. Lee, P.N. Kumta, Effects of grain refinement on the biocorrosion and in vitro bioactivity of magnesium, Mater. Sci. Eng. C. 57 (2015) 294–303, https://doi.org/10.1016/j.msec.2015.07.033.
[46] W. Bednarczyk, M. Wątroba, J. Kawałko, P. Bała, Determination of room-temperature superplastic asymmetry and anisotropy of Zn-0.8Ag alloy processed by ECAP, Mater. Sci. Eng. A 759 (2019) 55–58, https://doi.org/10.1016/j.msea.2019.05.029.
[47] W. Bednarczyk, M. Wątroba, J. Kawałko, P. Bała, Can zinc alloys be strengthened by grain refinement? A critical evaluation of the processing of low-alloyed binary zinc alloys using ECAP, Mater. Sci. Eng. A 748 (2019) 357–366, https://doi.org/10.1016/j.msea.2019.01.117.
[48] M. Larsson, A. Norlin, J. Weissenrieder, T. Karin, Degradation of zinc in saline solutions, plasma, and whole blood, J. Biomed. Mater. Res. Part B Appl. Biomater. 104B (2016) 1141–1151, https://doi.org/10.1002/jbm.b.33458.
[49] S. Zhao, J.M. Seitz, R. Eifler, H.J. Maier, R.J. Guillory, E.J. Earley, A. Drelich, J. Goldman, J.W. Drelich, Zn-Li alloy after extrusion and drawing: structural, mechanical characterization, and biodegradation in abdominal aorta of rat, Mater. Sci. Eng. C. 76 (2017) 301–312, https://doi.org/10.1016/j.msec.2017.02.167.
[50] C.S. Obayi, R. Tolouei, A. Mostavan, S. Turgeon, B.A. Okorie, D. Oray, D. Mantovani, Effect of grain sizes on mechanical properties and biodegradation behavior of pure iron for cardiovascular stent application, Biomatter 6 (2016) 1–9, https://doi.org/10.4161/21592527.2014.959874.
[51] J.C.T. Farge, Recrystallization of Zinc Alloys, McGill University Montreal, Canada, 1999.
[52] C. Wu, J. Labrie, Y.D.N. Tremblay, D. Haine, M. Mourez, M. Jacques, Zinc as an agent for the prevention of biofilm formation by pathogenic bacteria, J. Appl. Microbiol. 115 (2013) 30–40, https://doi.org/10.1111/jam.12197.
[53] C. Marambio-Jones, E.M.V. Hoek, A review of the antibacterial effects of silver nanomaterials and potential implications for human health and the environment, J. Nanopart. Res. 12 (2010) 1531–1551, https://doi.org/10.1007/s11051-010-9900-y.
[54] Y. Zhao, M. Ibrahim, W. Kan, G. Wu, C. Wang, Y. Zheng, K.W.K. Yeung, P.K. Chu, Enhanced antimicrobial properties, cytocompatibility, and corrosion resistance of plasma-modified biodegradable magnesium alloys, Acta Biomater. 10 (2014) 544–556, https://doi.org/10.1016/j.actbio.2013.10.012.